

Pulse self-compression to single-cycle pulse widths a few decades above the self-focusing threshold

A. A. Voronin and A. M. Zheltikov*

*Physics Department, International Laser Center, M.V. Lomonosov Moscow State University, Moscow 119992, Russia;**Department of Physics and Astronomy, Texas A&M University, 77843 College Station Texas, USA;**and Russian Quantum Center, 143025 Skolkovo, Moscow Region, Russia*

(Received 27 December 2015; published 11 August 2016)

We identify a physical scenario whereby optical-field waveforms with peak powers several decades above the critical power of self-focusing can self-compress to subcycle pulse widths. With beam breakup, intense hot spots, and optical damage of the material avoided within the pulse compression length by keeping this length shorter than the modulation-instability buildup length, the beam is shown to preserve its continuity at the point of subcycle pulse generation.

DOI: [10.1103/PhysRevA.94.023824](https://doi.org/10.1103/PhysRevA.94.023824)**I. INTRODUCTION**

Temporal self-compression is a universal behavior of ultrashort optical-field waveforms propagating in anomalously dispersive nonlinear media [1]. This phenomenon is often observed as a part of solitonic dynamics and is widely used for pulse compression in optical fibers [2]. With the advent of efficient and convenient parametric sources of ultrashort pulses in the midinfrared [3,4], the range where many solid-state materials exhibit anomalous dispersion, some of these pulse self-compression scenarios, earlier used primarily in the fiber-optic format, have been successfully extended to optical beams freely propagating in the bulk of transparent solids [5–10]. This regime of nonlinear pulse evolution in solids enables the generation of temporally compressible multi-octave midinfrared supercontinua [5,9,10] and opens the routes toward efficient all-solid-state sources of single-cycle and even subcycle pulses in the midinfrared [6,9,10].

If scaled to the energy level of tens of millijoules, these methods of pulse compression would ideally match the recently developed technology of short-pulse generation in the midinfrared based on optical parametric chirped-pulse amplification, which is capable of delivering sub-100-fs pulses at the subterawatt level of peak powers [11,12]. The solution of this problem, however, goes well beyond a mere scaling of the soliton regime of pulse compression. For subterawatt pulses now available in the midinfrared range [13], the level of peak powers would be several decades above the self-focusing threshold, $P_{cr} = C\lambda^2/(8\pi n_0 n_2)$, where C is a numerical factor ($C = 3.79$ for a Gaussian beam), λ is the wavelength, n_2 is the nonlinear index of refraction, and n_0 is the field-free index of refraction. In this regime, the temporal evolution of an ultrashort optical waveform cannot be considered independently of its spatial dynamics, because the beam becomes intrinsically unstable with respect to spatial modulation instabilities (MIs) [14], producing hot spots, breaking up into multiple filaments, eventually losing its continuity, connectedness, and spatial coherence. Ionization effects add to the complexity of spatiotemporal field dynamics [15,16], making the material prone to optical damage. With all these

factors being a part of the picture, the question arises as to whether any pulse-compression scenario is possible at all.

We show in this work that the answer to this question is affirmative. The most striking result of our analysis presented here is that, in spite of all the complexity of spatiotemporal field dynamics and the eventual inevitability of MI-induced beam breakup, physical scenarios whereby ultrashort pulses with peak powers P orders of magnitude higher than P_{cr} can be compressed to subcycle pulse widths can still be identified. Our $(3 + 1)$ -dimensional supercomputer simulations show that optical damage and excessive ionization effects can be avoided in this regime if the self-compression length is kept shorter than the spatial scale needed for the buildup of spatial MIs.

II. BASIC IDEAS AND QUALITATIVE CONSIDERATION

In their one-dimensional (1D) dynamics, observed in optical fibers, optical solitons propagating in media with an instantaneous cubic nonlinearity with no high-order dispersion are known to display well-resolved cycles [2], where the phase of pulse compression is followed by pulse stretching. The pulse-compression phase of this oscillatory dynamics is fully controlled by the soliton number $N = (l_d/l_{nl})^{1/2}$, where $l_d = (\tau/1.665)^2/|\beta_2|$, l_d is the dispersion length, $l_{nl} = \lambda(2\pi n_2 I)^{-1}$ is the nonlinear length, I is the field intensity, τ is the pulse full width at half maximum, and β_2 is the group-velocity dispersion coefficient. However, when the soliton pulse width τ approaches the field cycle and the peak power reaches the subterawatt level, optical shock waves, spatial self-action, and ionization make the field waveform dynamics drastically different from this textbook scenario.

The key physical idea behind our plan for self-compression in this extreme regime, with $P \gg P_{cr}$, is to avoid the generation of MI-induced hot spots across the beam as much as possible, thus preventing excessive photoionization in the medium. To this end, we keep the length l_c of maximum pulse self-compression in a nonlinear anomalously dispersive medium shorter than the typical length scale l_m within which spatial MIs tend to build up. In the basic physical model, solitonic self-compression is treated within the framework of the nonlinear Schrödinger equation (NSE) [2]. This model neglects all the non-NSE effects, such as inertia and dispersion of optical nonlinearity, high-order dispersion, and field-induced ionization. In this approximation, the minimum

*zheltikov@physics.msu.ru

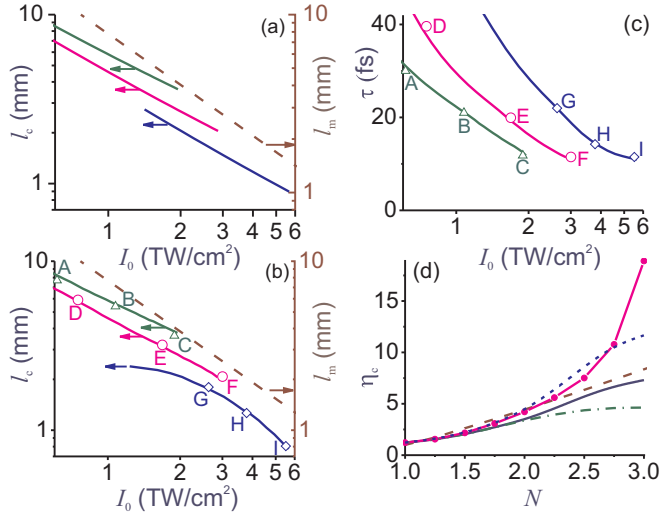


FIG. 1. The MI buildup length l_m (dashed line) and the optimal pulse-compression length l_c (solid lines) calculated by using (a) the NSE and (b) the one-dimensional (1D) GNSE as functions of field intensity. (c) The pulse width τ_c at the point of maximum compression as a function of field intensity calculated with the use of the 1D GNSE. The input pulse width is $\tau_0 = 80$ fs (blue), 150 fs (red), and 250 fs (green). Results of (3 + 1)-dimensional simulations are shown as circles, triangles, and diamonds. (d) The pulse-compression ratio $\eta = \tau_c/\tau_0$ calculated as a function of soliton number N for $\tau_0 = 80$ fs by using the NSE (dashed line) and the full 1D GNSE (solid line), 1D GNSE without ionization terms (dash-dotted line), 1D GNSE without HOKe terms (dotted line), and 1D GNSE with both ionization and HOKe terms disabled (filled circles connected by a solid line).

pulse width of a breathing soliton is achieved at the length $l_c \approx (\pi l_d/2)(0.32/N + 1.1/N^2)$ [2].

To estimate a typical scale l_m , we use the Bespalov–Talanov treatment of spatial MIs [14], which gives the following expression for the MI gain: $G = \exp(z/l_m)$. With the MI-induced multifilamentary structure across the beam building up from the level of noise, whose intensity is typically many orders of magnitude lower than the on-axis field intensity, we set $l_m = 5l_{nl}$ for a quantitative lower-bound estimate of the MI length in the $l_c < l_m$ criterion. Figure 1(a) compares the MI length scale l_m (the dashed line) with the NSE optimal

pulse-compression length l_c (solid lines), both calculated as a function of the field intensity. An important conclusion to be made from this comparison is that, for shorter pulses, the $l_c < l_m$ condition can be satisfied for higher field intensities and higher peak powers, allowing more powerful field waveforms to be compressed through this scenario while still avoiding dramatic MI buildup.

The solid lines in Figs. 1(b) and 1(c) present the optimal pulse-compression length l_c and the pulse width τ_c at $z = l_c$ as functions of field intensity for three values of the input pulse width τ_0 calculated by using the one-dimensional (1D) generalized nonlinear Schrödinger equation (GNSE) [2], including high-order dispersion, self-steepening, higher-order optical nonlinearities, and ionization effects. Along each curve in these plots, the input pulse width τ_0 is kept fixed, while the field intensity varies, leading to changes in the soliton number N . As can be seen from the comparison of Figs. 1(a) and 1(b), the soliton number N continues to be a meaningful parameter, controlling pulse self-compression even when all the relevant non-NSE effects are included in the model. Quantitatively, however, the key parameters of the self-compression scenario change. Most significantly, as GNSE calculations with ionization and high-order nonlinearities turned on and off show [Fig. 1(d)], the non-NSE effects tend to lower the compression ratio at the point of maximum pulse compression. At high field intensities, the electron density ρ , which builds up toward the back of the pulse, may also lead to optical damage when it approaches the critical electron density ρ_{cr} for radiation of given wavelength. In our analysis, we use the criterion $\rho = 0.1\rho_{cr}$ [15,16] to define the cutoff for the GNSE l_c curves in Figs. 1(a) and 1(b), setting a borderline for the considered pulse compression scenario in the region of high field intensities.

III. THE MODEL

We now address the central question of whether any scenario of pulse compression is physically feasible for peak powers many orders of magnitude above P_{cr} without the beam completely losing its connectedness and eventually the spatial coherence. To confront this problem, we resort to the three-dimensional time-dependent generalized nonlinear Schrödinger equation [15,16] for the amplitude of the field, which is referred to hereinafter as the (3 + 1)-dimensional GNSE model:

$$\begin{aligned} \frac{\partial}{\partial z} A(\omega, x, y, z) = & \left[\frac{ic}{2\omega n_0} \Delta_{\perp} + i\tilde{D}(\omega) \right] A(\omega, x, y, z) \\ & + \tilde{F} \left\{ i \frac{\omega_0 \tilde{T}}{c} [n_2 I(t, x, y, z) + n_4 I^2(t, x, y, z)] A(t, x, y, z) - \frac{U_i W}{2I} A(t, x, y, z) \right\} \\ & - \left(\frac{i\omega_0^2 \omega}{2cn_0 \rho_c (\omega^2 + \tau_c^{-2})} + \frac{\sigma(\omega)}{2} \right) \tilde{F}[\rho(t) A(t, x, y, z)]. \end{aligned}$$

Here, $A(t, x, y, z)$ is the field envelope, $A(\omega, x, y, z)$ is its Fourier transform, $I(t, x, y, z) = |A(t, x, y, z)|^2$ is the field intensity, x, y are the transverse coordinates, z is the coordinate along the propagation axis, t is the retarded time, $\omega = 2\pi c/\lambda$ is

the radiation frequency, λ is the wavelength, \tilde{F} is the Fourier transform operator, $\Delta_{\perp} = \partial^2/\partial x^2 + \partial^2/\partial y^2$ is the diffraction operator, $\tilde{D} = k(\omega) - k(\omega_0) - \partial k/\partial \omega|_{\omega_0}(\omega - \omega_0)$, ω_0 is the central frequency, $k(\omega) = \omega n(\omega)/c$, $n(\omega)$ is the refractive

index, $n_0 = n(\omega_0)$, n_2 and n_4 are the Kerr nonlinearity coefficients, $\tilde{T} = 1 + i\omega_0^{-1}\partial/\partial t$, ρ is the time-dependent electron density, $\rho_c = \omega_0^2 m_e \epsilon_0 / e^2$ is the critical electron density, $U_i = U_0 + U_{\text{osc}}$, U_i is the ionization potential, U_{osc} is the energy of field-induced electron oscillations, W is the photoionization rate, σ is the impact-ionization cross section, and e and m_e are the electron charge and mass, respectively.

This generalization of the NSE includes all the key physical phenomena that have been identified as significant factors behind the spatiotemporal evolution of ultrashort optical pulses in nonlinear media, such as dispersion and absorption of the medium, beam diffraction, Kerr nonlinearities, pulse self-steepening, spatial self-action phenomena, as well as ionization-induced loss, dispersion, and optical nonlinearities. In this model, the field evolution equation is solved jointly with the rate equation for the electron density $\rho(t)$,

$$\partial\rho/\partial t = W + \sigma(\omega_0)U_i^{-1}\rho I,$$

which includes photoionization with the photoionization rate calculated by using the Keldysh formalism [17] and impact ionization with the impact-ionization cross section calculated with the use of the Drude formula $\sigma(\omega) = e^2\tau_c[m_e\epsilon_0 n_0 c(1 + \omega^2\tau_c^2)]^{-1}$, where τ_c is the collision time.

Simulations are performed for typical parameters of a YAG crystal—a band gap of 6.4 eV, the Kerr-effect nonlinear refractive index $n_2 = 4 \times 10^{-16}$ cm²/W, and the higher-order Kerr effect (HOKE) coefficient $n_4 = -1 \times 10^{-29}$ cm⁴/W². Dispersion of YAG crystal was included in the model through a Sellmeier relation [18]. The zero group-velocity dispersion wavelength for YAG is $\lambda_z \approx 1610$ nm. Similar to many other suitable materials, YAG exhibits anomalous dispersion in the long-wavelength part of the near-IR and in the mid-IR range.

We therefore choose to work with an input field at a central wavelength $\lambda_0 = 3.9 \mu\text{m}$. Sub-100-fs pulses with peak powers orders of magnitude higher than the self-focusing threshold for YAG ($P_{cr} = 30$ MW at $\lambda_0 = 4 \mu\text{m}$) can be delivered at this central wavelength by midinfrared sources based on optical parametric chirped-pulse amplification. Spatial modulation instabilities leading to the formation of multiple filaments are seeded in our model by superimposing a Gaussian-noise modulation with a standard deviation of 3% on the input Gaussian beam profile [19]. Simulations were performed using an MPI parallel programming interface and the CUDA graphical architecture on the Lomonosov supercomputer cluster of Moscow State University.

IV. RESULTS AND DISCUSSION

A. Pulse self-compression

Results of (3 + 1)-dimensional GNSE simulations presented in Figs. 2–4 illustrate the key tendencies in pulse-envelope evolution and beam dynamics of an optical field in an anomalously dispersive nonlinear solid. As can be seen Figs. 2(a), 2(b), and 3(a), the pulse undergoes self-compression in the time domain at the first stage of its spatiotemporal dynamics ($z \leq l_c$), followed by a phase where the pulse experiences postcompression stretching in the time domain, while the beam breaks up into multiple filaments [to the right of the vertical dashed lines in Figs. 2(c) and 2(d)]. While the 1D treatment generally fails to describe this extreme scenario of pulse self-compression, within a limited area of parameter space, 1D GNSE calculations can still serve as a helpful guide for the (3 + 1)-dimensional analysis of pulse compression within a short propagation length $z \sim l_c$ as long

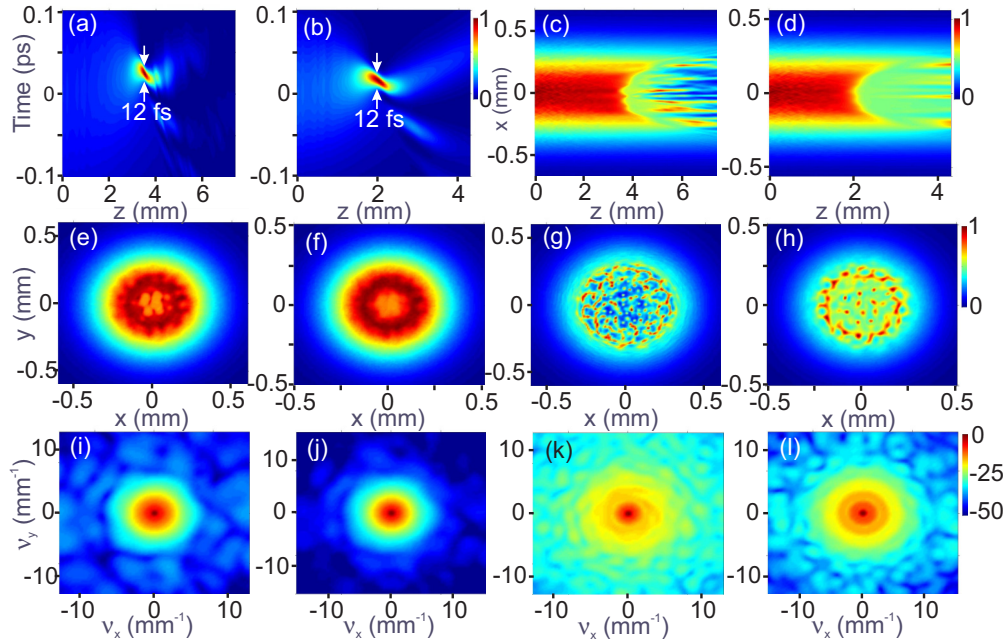


FIG. 2. Self-compression of laser pulses with the central wavelength $\lambda_0 = 3.9 \mu\text{m}$ and the input peak power $P_0 = 250P_{cr}$ in the regimes represented by points C and F in Figs. 1(b) and 1(c): (a), (b) spatiotemporal evolution, (c), (d) beam dynamics, (e)–(h) transverse beam profiles and (i)–(l) the angular spectra at the point of maximum pulse compression, (e), (i) $z = 3.7$ mm and (f), (j) 2.1 mm, and in the far field at (g), (k) $z = 7.4$ mm and (h), (l) 4.2 mm. The input pulse width and beam diameter are (a), (c), (e), (g), (i), (k) $\tau_0 = 80$ fs, $w_0 = 0.4$ mm and (b), (d), (f), (h), (j), (l) $\tau_0 = 150$ fs, $w_0 = 0.6$ mm.

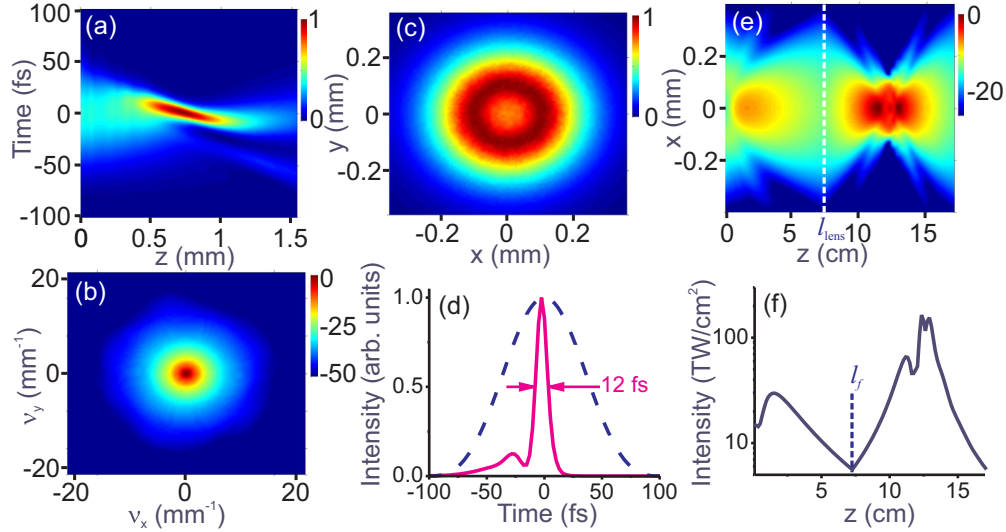


FIG. 3. Subcycle pulse generation by self-compression of laser pulses with $\lambda_0 = 3.9 \mu\text{m}$, initial pulse width $\tau_0 = 80 \text{ fs}$, beam diameter $w_0 = 0.4 \text{ mm}$, and input peak power $P_0 = 250P_{cr}$ in the regime represented by point I in Figs. 1(b) and 1(c): (a) spatiotemporal evolution, (b) transverse beam profile, (c) the angular spectra at the point of maximum pulse compression, $z = 0.75 \text{ mm}$, (d) temporal envelopes of the input pulse (dashed line) and the pulse at the point of maximum pulse compression (solid line), (e) two-dimensional map of beam dynamics and (f) one-dimensional profile of the field intensity in a vacuum behind a YAG plate with a thickness set exactly equal to l_c with a 2-cm-focal-length lens or mirror placed at a distance $l_f = 7 \text{ cm}$ from the exit surface (shown by the vertical dashed line).

as the diffraction length l_{df} is kept much longer than both l_c and l_m by an appropriate choice of the initial beam radius w_0 , input pulse width τ_0 , and input peak power P . In this regime, both diffraction-induced divergence and nonlinear dynamics are suppressed within l_c [Figs. 2(c) and 2(d)] and the minimum pulse width in $(3 + 1)$ -dimensional simulations is achieved at $z \approx l_c$, i.e., almost exactly at the point predicted by 1D GNSE. Moreover, in this regime, the 1D GNSE model provides a remarkably high accuracy in its predictions of the pulse width τ_c at the point of maximum pulse compression [Fig. 1(c)]. This close agreement between the one- and $(3 + 1)$ -dimensional models is demonstrated in Figs. 1(b) and 1(c), where the points of maximum pulse compression in $(3 + 1)$ -dimensional simulations (circles, triangles, and diamonds) are shown against the results of 1D modeling (solid lines). As can be seen from these plots, predictions of one- and $(3 + 1)$ -dimensional simulations for l_c agree very well within a broad range of parameters as long as the conditions $l_c \ll l_{df}$ and $l_c < l_m$ are satisfied and ionization does not lead to a dramatic scattering of the optical beam within l_c .

With the length l_c chosen very close to l_m in our modeling, to provide the largest MI-free propagation length and, thus, the highest efficiencies of pulse compression, modulation instabilities lead to a rapid breakup of the beam into multiple filaments beyond the $z = l_c$ point [Figs. 2(c), 2(d), and 4(f)–4(h)]. At $z \approx 2l_c$, the laser beam, as can be seen from Figs. 2(g) and 2(h), has already lost its connectedness and exhibits a random array of hot spots across its cross section.

B. Multiple filamentation

To examine the influence of growing MIs on the quality of the laser beam at the point of maximum pulse compression, we use our $(3 + 1)$ -dimensional model to calculate the beam profiles and the angular spectra of the laser field at $z = l_c$

for nine sets of input field parameters represented by points A to I in Figs. 1(b) and 1(c). All these points correspond to the input peak power $P_0 = 250P_{cr}$. They all fall within the $l_c < l_m$ domain, but lie close to the $l_c = l_m$ borderline, beyond which the laser beam tends to breakup before the field reaches the point of maximum pulse compression. Thus, although all these sets of input parameters enable pulse self-compression to subcycle pulse widths [Figs. 2(a), 2(b), 3(a), and 3(d)] without dramatic beam degradation [Figs. 2(e), 2(f), 2(i), 2(j), 3(b), and 3(c)], well-resolved MI signatures tend to gradually build up in the transverse beam profiles and the angular spectra of the laser field as the optimal pulse compression length l_c for a given set of input parameters approaches l_m . These signatures are clearly seen in the transverse beam profiles at the point of maximum pulse compression for the regimes represented by points C and F [Figs. 2(e) and 2(f)] and especially in the angular spectra of these beams [Figs. 2(i) and 2(j)], which give the beam patterns in the far field if plotted in the $v_x = x/(\lambda_0 D)$ and $v_y = y/(\lambda_0 D)$ coordinates, D being the distance to the observation point in the far field and x and y being the transverse coordinates.

The optimal pulse-compression point I, however, lies further away from the $l_c = l_m$ borderline in Fig. 1(b) than the C and F points. Moreover, among all nine points in Figs. 1(b) and 1(c), the I point ($P_0 = 250P_{cr}$, $\tau_0 = 80 \text{ fs}$, $w_0 \approx 0.21 \text{ mm}$, $l_{df} \approx 130 \text{ mm}$, $l_{nl} \approx 0.27 \text{ mm}$, $l_d \approx 2.4 \text{ mm}$) represents the case of the shortest optimal pulse-compression length, $l_c \approx 0.75 \text{ mm}$, which helps avoid MI-induced beam perturbation to a maximum extent.

C. Subcycle field waveforms

Both 1D calculations and $(3 + 1)$ -dimensional simulations predict that an extremely short, subcycle field waveforms can be generated through the pulse self-compression scenario

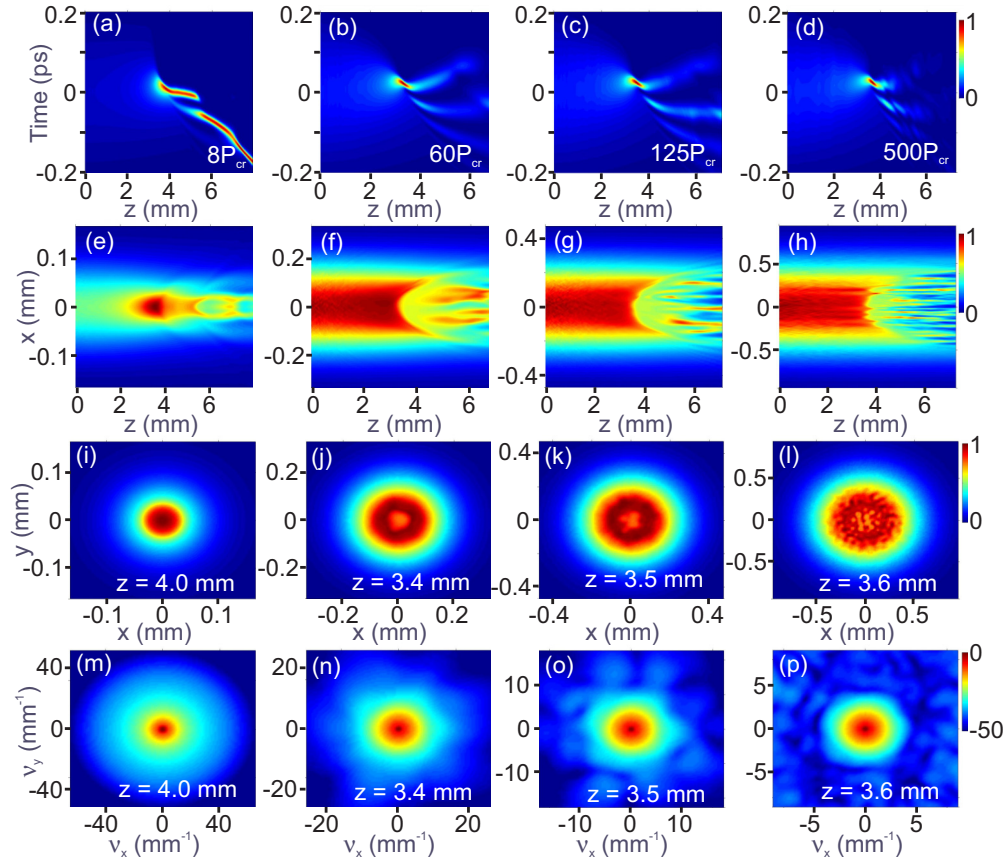


FIG. 4. Subcycle pulse generation by self-compression of laser pulses with $\lambda_0 = 3.9 \mu\text{m}$ and the initial pulse width $\tau_0 = 250 \text{ fs}$ in an anomalously dispersive nonlinear medium: (a)–(d) spatiotemporal evolution, (e)–(h) beam dynamics, (i)–(l) transverse beam profiles, and (m)–(p) the angular spectra at the point of maximum pulse compression. The input peak power of the laser pulse and beam diameter are (a), (e), (i), (m) $P_0 = 8P_{cr}$, $w_0 = 0.17 \text{ mm}$ (b), (f), (j), (n) $60P_{cr}$, $w_0 = 0.35 \text{ mm}$, (c), (g), (k), (o) $125P_{cr}$, $w_0 = 0.5 \text{ mm}$, and (d), (h), (l), (p) $500P_{cr}$, $w_0 = 1.0 \text{ mm}$.

represented by this point [Figs. 3(a) and 3(d)]. The (3 + 1)-dimensional simulations also show that, because l_c is so short in this case, such extremely short pulses can be produced without a dramatic beam degradation. Neither the transverse beam profile [Fig. 3(b)] nor the angular spectrum [Fig. 3(c)] displays any significant signatures of MI-induced hot spots at this point.

The temporal envelope of the pulse produced at this point [solid line in Fig. 3(d)] features a central peak with a pulse width $\tau \approx 12 \text{ fs}$, which corresponds to 0.9 field cycles at the carrier wavelength $\lambda_0 = 3.9 \mu\text{m}$. This main peak in the pulse envelope is preceded by a pedestal, which contains 23% of the total energy of the compressed pulse and whose peak intensity as approximately 14 times lower than the intensity at the center of the 12 fs main peak. The peak power achieved within this peak is 20 GW, i.e., 2.5 times higher than the input peak power. With the thickness of the nonlinear medium set exactly equal to l_c , a 2-cm-focal-length lens or mirror placed at a distance of 7 cm from the exit surface will focus this beam into a spot with a diameter of about $85 \mu\text{m}$ [Fig. 3(e)], giving rise to a field intensity of 165 TW/cm^2 at the focal plane [Fig. 3(f)].

Figure 4 presents (3 + 1)-dimensional simulations demonstrating that subcycle field waveforms with a pulse width of

12 to 13 fs can be generated [see also Fig. 1(c)] through the above-identified regime of pulse self-compression within a sufficiently broad range of parameters for input peak powers up to $500P_{cr}$. In these simulations, we fix the input pulse width at $\tau_0 = 250 \text{ fs}$ and adjust the input beam diameter in such a way as to achieve the generation of subcycle pulses at the point of maximum pulse self-compression within the broadest possible range of input peak powers P_0 . Simulations presented in Fig. 4 verify the key tendencies in the spatiotemporal dynamics of ultrashort pulses revealed by the analysis above. Most importantly, the beam preserves its continuity up to the point of maximum pulse compression [Figs. 4(e)–4(h)], which varies from 3.5 to 4.0 mm in calculations presented in Fig. 4, depending on the input parameters. The beam, however, tends to break up into multiple filaments due to MIs, losing its continuity and, eventually, coherence beyond the $z = l_c$ point [Figs. 4(f)–4(h)].

V. CONCLUSION

To summarize, we demonstrated through a numerical analysis of the (3 + 1)-dimensional generalized nonlinear Schrödinger equation that ultrashort pulses with peak powers P orders of magnitude higher than P_{cr} can be compressed

to subcycle pulse widths as a part of their spatiotemporal evolution in an anomalously dispersive nonlinear medium, While MI-induced beam breakup into multiple filaments is eventually inevitable at this level of peak powers, optical damage and excessive ionization effects can be avoided in this regime, as our (3 + 1)-dimensional supercomputer simulations show, by keeping the self-compression length shorter than the spatial scale needed for the buildup of spatial modulation instabilities.

ACKNOWLEDGMENTS

This research was supported in part by the Russian Foundation for Basic Research (Projects No. 14-29-07182, No. 15-32-20713, No. 14-22-02105, and No. 16-02-00843) the Welch Foundation (Grant No. A-1801) and ONR (Award No. N00014-16-1-2578). Research into the nonlinear optics in the midinfrared has been supported by the Russian Science Foundation (Project No. 14-12-00772).

-
- [1] Y.-R. Shen, *The Principles of Nonlinear Optics* (Wiley-Interscience, New York, 1984).
- [2] G. P. Agrawal, *Nonlinear Fiber Optics* (Academic Press, San Diego, 2001).
- [3] R. A. Kaindl, M. Wurm, K. Reimann, P. Hamm, A. M. Weiner, and M. Woerner, *J. Opt. Soc. Am. B* **17**, 2086 (2000).
- [4] A. A. Lanin, A. A. Voronin, E. A. Stepanov, A. B. Fedotov, and A. M. Zheltikov, *Opt. Lett.* **39**, 6430 (2014).
- [5] F. Silva, D. Austin, A. Thai, M. Baudisch, M. Hemmer, D. Faccio, A. Couairon, and J. Biegert, *Nat. Commun.* **3**, 807 (2012).
- [6] M. Hemmer, M. Baudisch, A. Thai, A. Couairon, and J. Biegert, *Opt. Express* **21**, 28095 (2013).
- [7] M. Durand, A. Jarnac, A. Houard, Y. Liu, S. Grabielle, N. Forget, A. Durécu, A. Couairon, and A. Mysyrowicz, *Phys. Rev. Lett.* **110**, 115003 (2013).
- [8] A. Pugžlys, P. Malevich, S. Alisauskas, A. A. Voronin, D. Kartashov, A. Baltuska, A. Zheltikov, and D. Faccio, in *Technical Digest of Conference on Lasers and Electro-Optics* (Optical Society of America, Washington DC, 2014), pp. FTh1D–3.
- [9] A. A. Lanin, A. A. Voronin, E. A. Stepanov, A. B. Fedotov, and A. M. Zheltikov, *Opt. Lett.* **40**, 974 (2015).
- [10] H. Liang, P. Krogen, R. Grynko, O. Novak, C.-L. Chang, G. J. Stein, D. Weerawarne, B. Shim, F. X. Kärtner, and K.-H. Hong, *Opt. Lett.* **40**, 1069 (2015).
- [11] T. Popmintchev, M.-C. Chen, D. Popmintchev, P. Arpin, S. Brown, S. Ališauskas, G. Andriukaitis, T. Balčiunas, O. D. Mücke, A. Pugžlys, A. Baltuška, B. Shim, S. E. Schrauth, A. Gaeta, C. Hernández-García, L. Plaja, A. Becker, A. Jaron-Becker, M. M. Murnane, and H. C. Kapteyn, *Science* **336**, 1287 (2012).
- [12] A. V. Mitrofanov, A. A. Voronin, D. A. Sidorov-Biryukov, A. Pugžlys, E. A. Stepanov, G. Andriukaitis, T. Flöry, S. Ališauskas, A. B. Fedotov, A. Baltuška, and A. M. Zheltikov, *Sci. Rep.* **5**, 8368 (2015).
- [13] A. V. Mitrofanov, A. A. Voronin, S. I. Mitryukovskiy, D. A. Sidorov-Biryukov, A. Pugžlys, G. Andriukaitis, T. Flöry, E. A. Stepanov, A. B. Fedotov, A. Baltuška, and A. M. Zheltikov, *Opt. Lett.* **40**, 2068 (2015).
- [14] V. I. Bespalov and V. I. Talanov, *ZhETF Pis. Red.* **3**, 471 (1966) [*JETP Lett.* **3**, 307 (1966)].
- [15] A. Couairon and A. Mysyrowicz, *Phys. Rep.* **441**, 47 (2007).
- [16] L. Bergé, S. Skupin, R. Nuter, J. Kasparian, and J.-P. Wolf, *Rep. Prog. Phys.* **70**, 1633 (2007).
- [17] L. V. Keldysh, *Zh. Eksp. Teor. Fiz.* **47**, 1945 (1964) [*Sov. Phys. JETP* **20**, 1307 (1965)].
- [18] D. E. Zelmon, D. L. Small, and R. Page, *Appl. Opt.* **37**, 4933 (1998).
- [19] A. A. Voronin, A. M. Zheltikov, T. Ditmire, B. Rus, and G. Korn, *Opt. Commun.* **291**, 299 (2013).